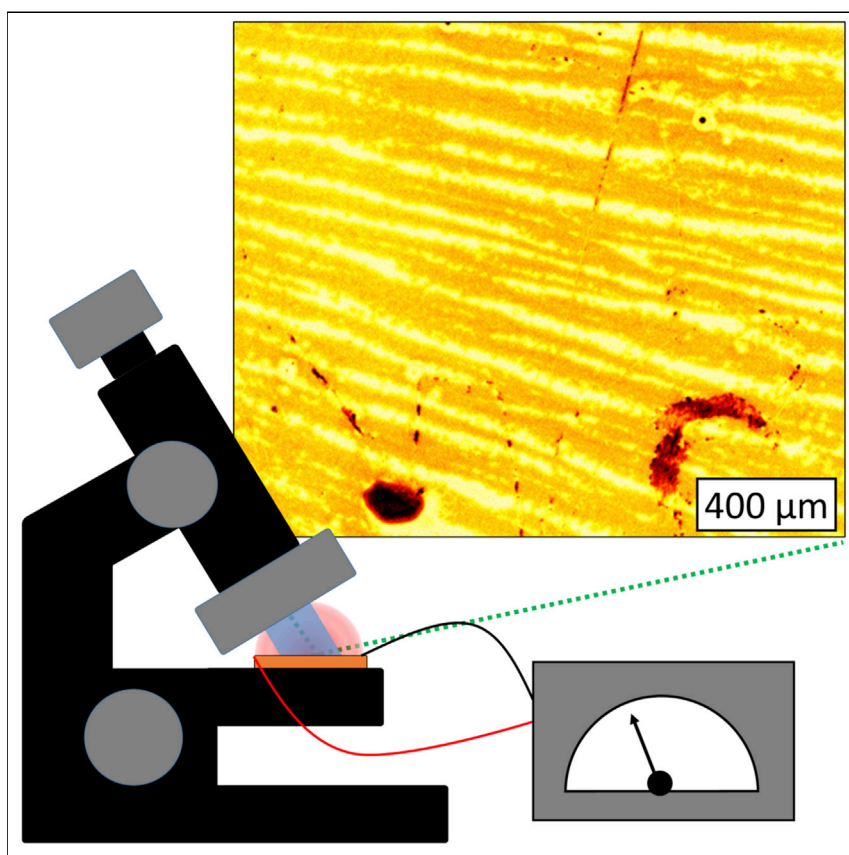


Article

Revealing fundamentals of charge extraction in photovoltaic devices through potentiostatic photoluminescence imaging



A method to determine local photocurrent-voltage curves of solar cells by potentiostatic photoluminescence imaging (PPI) is derived from basic principles and examined by close-to-ideal III-V as well as high-efficient perovskite solar cells. The real-time assessment of the local charge extraction allows relating morphological artifacts to device performance and loss mechanisms such as electrical coupling at interfaces and surface recombination at a microscopic resolution.

Lukas Wagner, Patrick Schygulla, Jan Philipp Herterich, ..., Michael Grätzel, Andreas Hinsch, Stefan W. Glunz

lukas.wagner@physik.uni-marburg.de (L.W.)
yuhang.liu@epfl.ch (Y.L.)
andreas.hinsch@ise.fraunhofer.de (A.H.)

Highlights

A method for electrical-bias-dependent photoluminescence microscopy is introduced

The method enables imaging of the local photocurrent in solar cells

Time-resolved charge-extraction imaging is demonstrated for perovskite solar cells

Electrical coupling at interfaces and surface recombination is revealed



Understanding

Dependency and conditional studies on material behavior

Wagner et al., Matter 5, 1–13
July 6, 2022 © 2022 The Authors. Published by Elsevier Inc.
<https://doi.org/10.1016/j.matt.2022.05.024>

Article

Revealing fundamentals of charge extraction in photovoltaic devices through potentiostatic photoluminescence imaging

Lukas Wagner,^{1,2,3,7,*} Patrick Schygulla,¹ Jan Philipp Herterich,^{1,4} Mohamed Elshamy,¹ Dmitry Bogachuk,^{1,2} Salma Zouhair,^{1,5} Simone Mastroianni,^{1,4} Uli Würfel,^{1,4} Yuhang Liu,^{6,*} Shaik M. Zakeeruddin,⁶ Michael Grätzel,⁶ Andreas Hinsch,^{1,*} and Stefan W. Glunz^{1,2}

SUMMARY

The photocurrent density-voltage ($J(V)$) curve is the fundamental characteristic to assess opto-electronic devices, in particular solar cells. However, it only yields information on the performance integrated over the entire active device area. Here, a method to determine spatially resolved photocurrent images by voltage-dependent photoluminescence microscopy is derived from basic principles. The opportunities and limitations of the approach are studied by the investigation of III-V and perovskite solar cells. This approach allows the real-time assessment of the microscopically resolved local $J(V)$ curve and the steady-state J_{sc} as well as transient effects. In addition, the measurement contains information on local charge extraction and interfacial recombination. This facilitates the identification of regions of non-ideal charge extraction and enables linking these to the processing conditions. The proposed technique highlights that, combined with potentiostatic measurements, luminescence microscopy can be a powerful tool for the assessment of performance losses and the improvement of solar cells.

INTRODUCTION

The current density-voltage ($J(V)$) curve builds the basis of any further characterization and improvement of solar cells and other opto-electronic devices. This characteristic provides a broad range of information on the fundamental mechanisms such as charge-carrier generation, recombination, and transport losses. Conventionally, the $J(V)$ curve is measured by illuminating the full device and externally probing the current flowing between the electrodes with a source meter. This approach therefore only provides information integrated over the entire device area. A range of techniques have been established for spatially resolved analysis of photovoltaic devices^{1,2} such as light-beam-induced current mapping (LBIC),^{3–5} lock-in thermography (LIT),^{6–8} photoluminescence (PL) imaging,^{3,9–24} and electroluminescence (EL) imaging.²⁵ However, as further discussed in the [supplemental information](#) (section A), these techniques can either probe only a portion of the local $J(V)$ characteristics or require numerical fitting to a postulated diode model. Moreover, for perovskite solar cells (PSCs), scanning probe microscopy has been demonstrated to yield valuable information on the local photocurrent below the optical resolution limit.^{26–29} Thus, it is especially crucial for emerging photovoltaic (PV) technologies like PSCs to gain spatially resolved fundamental information about the charge transport and

Progress and potential

Spatial characterization methods are essential for a deeper understanding of physical phenomena and quality control of opto-electric devices such as solar cells. Here, a method to derive local photocurrent images by electrical-bias-dependent photoluminescence microscopy is presented. As derived from basic principles, the method is based on the phenomenon of photoluminescence quenching as charge carriers are externally extracted. It is demonstrated for III-V and perovskite solar cells that the approach enables a real-time assessment of the spatially resolved charge extraction. This allows us to identify performance-loss mechanisms such as electrical interconnection at the interfaces or surface recombination at microscopic resolution.

the extraction phenomena on the microscopic as well as on the macroscopic scale to further enhance the power-conversion efficiency and long-term stability of these cells. Therefore, novel advanced characterization techniques are necessary.

The physics of optoelectronic devices can be divided into fundamental operation processes. For PV power generation, these are the photogeneration of charge carriers by the absorption of photons, the transport to and separation of the photogenerated electrons and holes at charge-extraction layers (CELs), and the extraction into the outer device terminals (cables). The three processes have been described by so-called reciprocity relations by Donolato,³⁰ Rau,³¹ and Wong and Green,³² respectively. To each of these processes, fundamental loss mechanisms can be assigned, namely optical and absorption losses, radiative and non-radiative recombination mechanisms, and transport losses.

In this work, we introduce a method based on electrical-bias-dependent PL imaging that allows the immediate determination of the charge-extraction efficiency of photogenerated charge carriers. The approach makes use of the observation that the difference between two PL images at different bias voltages yields direct spatially resolved information on the local $J(V)$. We propose to refer to this method as local charge-extraction analysis as “potentiostatic photoluminescence imaging” (PPI). We outline the theoretical principles of the PPI approach and experimentally demonstrate the validity by means of a close-to-ideal GaInAsP solar cell. Next, we show its potential to spatially characterize regions of PSCs with high power-conversion efficiency (PCE >20%) in terms of their charge-extracting ability by investigating both microscopic images of the local short-circuit current density J_{sc} in steady state as well as local $J(V)$ curves. Based on these results, we demonstrate how distinct charge-extraction signatures of the PPI method can be linked to physical properties of the perovskite layer, the CELs, and the respective interfaces.

Theory

The PPI method is based on a detailed-balance approach, considering that in steady state, the current density measured at the outer solar cell contacts, $J(V)$, can be expressed by the current density of the photogenerated charge carriers, J_{gen} , and the (internal) recombination in the perovskite layer and at respective interfaces, $J_{rec}(V)$,

$$J(V) = J_{gen} - J_{rec}(V). \quad (\text{Equation 1})$$

Here, we assume that in the considered operation range ($0 \text{ V} \leq V \leq V_{oc}$; open-circuit voltage [V_{oc}]), the internal generation current J_{gen} is not affected by the applied bias. Moreover, without loss of generality, we assume that the photon flux to illuminate the sample is constant over time and spatially homogeneous.

The internal recombination processes comprise non-radiative and radiative components, $J_{n.r.}$ and J_{rad} , respectively: $J_{rec} = J_{n.r.} + J_{rad}$. They can be related to each other using a proportionality factor k by

$$J_{n.r.}(V) = k(V) \cdot J_{rad}(V). \quad (\text{Equation 2})$$

Equation (2) is generally valid if k is a function of the applied bias, $k = k(V)$. Here, we show that if the probed sample has a diode ideality factor close to one and displays negligible resistive losses (high parallel resistance, low series resistance), then it is justified to assume a linear relationship between $J_{n.r.}(V)$ and $J_{rad}(V)$ and, hence, $k = \text{const.}$, which we will assume in the following. Empirical indications for the validity of this assumption in PSCs have already been presented by Stolterfoht and

¹Fraunhofer Institute for Solar Energy Systems ISE, Heidenhofstraße 2, 79110 Freiburg, Germany

²Laboratory for Photovoltaic Energy Conversion, University of Freiburg, Emmy-Noether-Straße 2, 79110 Freiburg, Germany

³Physics of Solar Energy Conversion Group, Department of Physics, Philipps-University Marburg, Renthof 7, 35032 Marburg, Germany

⁴Freiburg Materials Research Center FMF, University of Freiburg, Stefan-Meier-Straße 21, 79104 Freiburg, Germany

⁵ERCMN, FSTT, Abdelmalek Essaadi University, Tetouan, Morocco

⁶Laboratory of Photonics and Interfaces (LPI), Department of Chemistry and Chemical Engineering, École Polytechnique Fédérale de Lausanne, 1015 Lausanne, Switzerland

⁷Lead contact

*Correspondence: lukas.wagner@physik.uni-marburg.de (L.W.), yuhang.liu@epfl.ch (Y.L.), andreas.hinsch@ise.fraunhofer.de (A.H.)

<https://doi.org/10.1016/j.matt.2022.05.024>

coworkers.²¹ A detailed theoretical discussion of this assumption as well as a general expression are presented in the [supplemental information](#) (sections B, C, and D).

Now, [Equation \(1\)](#) can be expressed as

$$J(V) = J_{\text{gen}} - (1 + k) \cdot J_{\text{rad}}(V). \quad (\text{Equation 3})$$

$J_{\text{rad}}(V)$ can be related to the signal of a photodetector $S_{\text{PL}}(V)$ by

$$S_{\text{PL}}(V) = c \frac{J_{\text{rad}}(V)}{e}, \quad (\text{Equation 4})$$

where e is the elementary charge and c describes the probability that photons generated by radiative recombination enter the detector area and are translated into a detector signal.

Using [Equations \(3\) and \(4\)](#), we can now relate the electrical photocurrent to the difference between the voltage-dependent PL intensity $PL(V)$ and the PL at open circuit, $PL(V_{\text{oc}})$. By normalizing the term, the expression becomes independent of setup-specific factors, which makes the technique independent from elaborate calibration measures. We find that

$$\frac{S_{\text{PL}}(V_{\text{oc}}) - S_{\text{PL}}(V)}{S_{\text{PL}}(V_{\text{oc}})} = \frac{J(V)}{J_{\text{gen}}}. \quad (\text{Equation 5a})$$

This relation shows that PL microscopy can be used to derive spatially as well as time-resolved images of the local $J(V)$ performance of a PV device. Two applications are especially interesting: first, by recording only two PL images, one at open circuit and one at short circuit, the image of the local short-circuit photocurrent density J_{sc} can be derived. Second, by recording PL images at various voltages, the local $J(V)$ of specific spots on the cell can be investigated. These approaches are investigated in the following. Thereby, the $J(V)/J_{\text{gen}}$ results determined by PL microscopy will be denoted as $J(V)/J_{\text{gen}}|_{\text{PL}}$.

For samples that display non-ideal diode behavior, such as the PSC devices studied below, assumptions made in [Equation \(3\)](#) cannot be strictly applied, and the ratio between the PL signals is only an approximation of the normalized local photocurrent (cf., the detailed discussion in the [supplemental information](#), sections B and C). Therefore, for such samples, we suggest using the term “charge-extraction coefficient”, $c_{\text{ex}}(V)$, with

$$c_{\text{ex}}(V) = \frac{S_{\text{PL}}(V_{\text{oc}}) - S_{\text{PL}}(V)}{S_{\text{PL}}(V_{\text{oc}})} \approx \frac{J(V)}{J_{\text{gen}}}. \quad (\text{Equation 5b})$$

RESULTS AND DISCUSSION

Experimental validation of the PPI approach

III-V-based PV device

Many III-V compound semiconductors, such as gallium-arsenide (GaAs), indium-phosphide (InP), or combinations like $\text{Ga}_x\text{In}_{1-x}\text{As}_y\text{P}_{1-y}$, have a direct band gap. Hence, for III-V semiconductor crystals with a low defect density, radiative recombination is the dominant recombination mechanism. In addition, the high absorption coefficient allows using thin absorber layers in the order of a few micrometers. This fact, along with sufficiently high charge-carrier mobilities and lifetimes, promises high PCEs of this material class in PV applications.^{33,34} III-V compound semiconductors can be grown epitaxially with high crystal quality using, for instance, metalorganic vapor-phase epitaxy (MOVPE). The highest efficiencies of both single- and multi-junction solar cells under the AM1.5 g solar spectrum and under

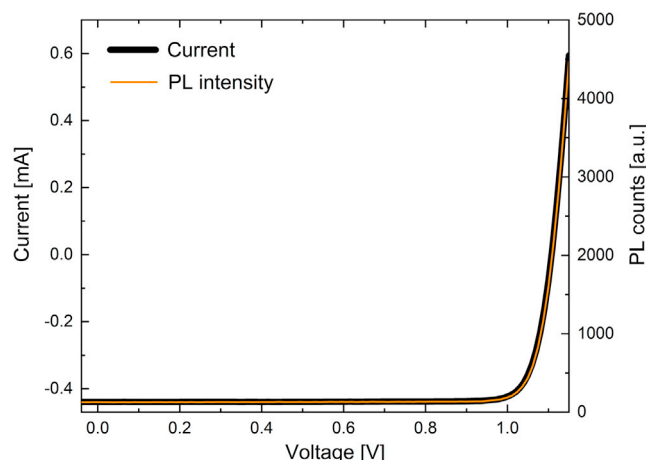


Figure 1. $I(V)$ and $PL(V)$ characteristic of a close-to-ideal III-V solar cell

Current-voltage curve of a highly efficient (18.7% power-conversion efficiency)

$\text{Ga}_{0.91}\text{In}_{0.09}\text{As}_{0.83}\text{P}_{0.17}$ solar cell (thick black line), compared with the simultaneously recorded $PL(V)$ measurement (thin orange line).

concentration were achieved with III-V based devices, reaching efficiencies as high as 47.1%.^{35–37}

To test the assumptions made in Equation (3), a $\text{Ga}_{0.91}\text{In}_{0.09}\text{As}_{0.83}\text{P}_{0.17}$ solar cell with almost ideal PV properties in terms of diode behavior and transport losses, as derived from a one-diode model fit to a measured current-voltage characteristic, was studied (cf., Figure S5 in the supplemental information, section E). Figure 1 displays the current voltage characteristic of this III-V semiconductor device and the simultaneously recorded $PL(V)$ curve. The remarkable overlap of these measurements highlights the validity of the above outlined theoretical considerations.

By applying a baseline correction considering the reflectance of the sample, at short circuit ($J(0) = J_{sc}$), the charge-extraction efficiency $J_{sc}/J_{gen}|_{PL}$ is assessed to be 0.87 ± 0.03 from the PPI measurements. To validate this result, the internal quantum efficiency (IQE) was determined by a direct measurement of the external quantum efficiency (EQE) and the reflectance of the device at a wavelength of 620 nm, close to the excitation wavelength of the PPI setup of 623 nm. The IQE amounted to 0.98 ± 0.05 (cf., Figure S6). The discrepancy of 11 %_{abs} can be partially attributed to measurement errors that occurred from the involvement of multiple characterization methods (details of the error estimation can be found in the supplemental information, section I-3). Additionally, we observed a non-linear signal offset as well as spatial inhomogeneities in the PL microscopy system that induce additional uncertainties (cf., supplemental information, section I-4). Due to hardware constraints, no four-point configuration was used for the PPI measurement, introducing additional series resistances by the contact needles and wiring. Moreover, the sample was contacted with micromanipulators, which may have introduced additional contact resistances. These parasitic external series resistances of the PPI setup may be another reason for the lower charge $J_{sc}/J_{gen}|_{PL}$ value compared with the IQE value. Overall, while there remain multiple opportunities to further improve the measurement method, the results show that the PPI approach is in line with the theoretical predictions.

Perovskite-based PV device

Monocrystalline, wafer-based PV devices like III-V solar cells typically display very homogeneous PL over the active device area (cf., Figure S7). In contrast to that,

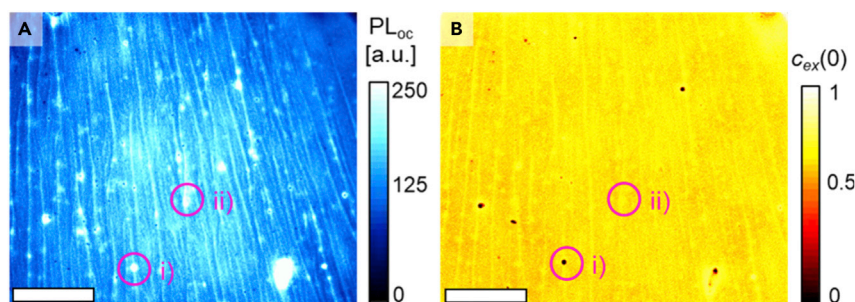


Figure 2. Charge-extraction image of a perovskite solar cell

(A and B) $PL(V_{oc})$ (A) and $c_{ex}(0)$ (B) determined from two PL images at open and short circuits of a high-performing (power-conversion efficiency [PCE] >20%) perovskite solar cell. The device was illuminated with a red LED (632 nm). The scale bar corresponds to 400 μm in both images.

even highly efficient PSCs show significant local heterogeneities.³⁸ To assess the full potential of microscopically resolved charge-extraction imaging by the PPI approach, measurements were carried out on a high-efficiency PSC with a layer structure of glass/fluorine-doped tin oxide (FTO)/compact titanium dioxide (TiO_2)/mesoporous TiO_2 /perovskite/Spiro-OMeTAD/Au using a perovskite consisting of $\text{FA}_{0.92}\text{MA}_{0.04}\text{Cs}_{0.04}\text{PbI}_3$ with additional $(\text{PbI}_2)_{0.067}$ (cf., [supplemental information](#), section F, for processing details). Stabilized measurements of the J-V parameters under AM1.5 g illumination yielded a stabilized PCE of 21.2%, a stabilized J_{sc} of 26.4 mA/cm^2 , and a stabilized V_{oc} of 1.03 V (cf., [Figure S9](#)).

Despite the high performance, the microscopic PL image of the device recorded at open-circuit conditions ($PL(V_{oc})$) shown in [Figure 2A](#) displays a highly inhomogeneous active area. The image reveals morphological features that are typically assigned to perovskite films formed by spin coating such as stripes and dots. In regions of highest $PL(V_{oc})$, such as in features (i) and (ii), the PL intensity exceeds that of the surrounding area by more than a factor of five. [Figure 2B](#) displays the image of the local charge-extraction coefficient assessed by PPI measurements in steady state, i.e., after stabilizing the devices for longer than 60 s. As can be seen in the $c_{ex}(0)$ image, it can be misleading to directly conclude from the $PL(V_{oc})$ image on the local device performance. In the $c_{ex}(0)$ representation, the active area is comparatively more homogeneous and will reveal more meaningful information on the aforementioned morphological patterns. Concerning regions of high $PL(V_{oc})$, the PPI method allows to distinguish between two distinct features: feature (i) displays a spot with very low $c_{ex}(0)$, i.e., the PL intensity is not quenched when switching from open- to short-circuit conditions. While the high $PL(V_{oc})$ is an indicator for the presence of high-quality perovskite crystals with low non-radiative recombination, the low $c_{ex}(0)$ suggests a poor electrical connection of the perovskite to the CELs. A similar behavior was recently also observed by Soufiani et al., who demonstrated by a method employing inhomogeneous illumination that high PL (i.e., low non-radiative recombination) and a low EL signal (i.e., poor charge-carrier injection) is indicative of high series resistances.³⁹ In contrast, feature (ii) displays both high $PL(V_{oc})$ and high $c_{ex}(0)$ due to a benign electrical coupling.

A systematic comparison of LBIC, EL, PL, and PPI measurements on PSC samples is outlined in the [supplemental information](#) (section H), demonstrating that the PPI approach adds valuable additional insights or complementary findings to the information provided by established characterization techniques. Moreover, a detailed discussion on experimental limitations of the PPI approach and calibration strategies

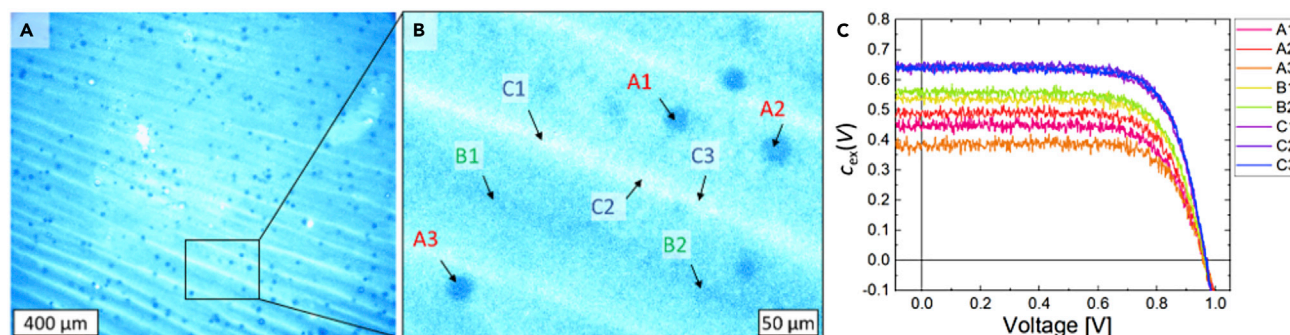


Figure 3. PL(V)-based current-voltage imaging

(A and B) $PL(V_{oc})$ intensity map of a sample in open circuit (A) and close-up of a selected area (B).

(C) Local $c_{ex}(V)$ curves of the spots highlighted in (B) for a slow reverse voltage scan (20 mV/s). The sample was illuminated with a 632 nm LED light. The scale bars correspond to 400 μm and 50 μm in images (A) and (B), respectively.

can be found in the [supplemental information](#), section I, along with an estimate of the diode model parameters in [Figures S18A–S18C](#).

J(V) imaging

[Figure 3A](#) shows the microscopic $PL(V_{oc})$ image of another PSC, displaying similar patterns as the sample discussed above. The patterns were grouped according to the pattern type and PL intensity in the $PL(V_{oc})$ image: dots (A) and stripe patterns (B) with lower $PL(V_{oc})$ as well as stripes with higher $PL(V_{oc})$ (C) (cf., [Figure 3B](#), magnified image). With the PPI method, we can retrieve the local $c_{ex}(V)$ curve for each pixel of the microscope image. [Figure 3C](#) shows the corresponding $c_{ex}(V)$ curves for the features A, B, and C (cf. [supplemental information](#), section J, for further details). One can see that the similarities from the $PL(V_{oc})$ images are also found in the $c_{ex}(V)$ representation, where the J_{sc} is highest for features C, lower for B, and lowest for A. This demonstrates the potential to directly record the local $c_{ex}(V)$ image with microscopic resolution.

At this point, it is important to note that the PPI method implicitly assumes that the V_{oc} is equal over the entire cell area. This assumption is only valid if the absorber is well coupled to the outer electrodes and if the sheet resistivity of the electrodes is low. Finally, it is important to take the unique transient behavior of perovskite material into account for any luminescence measurement.²⁵ For PSCs, reaching a stabilized state after changes in electrical bias, illumination, or even atmospheric conditions can require minutes to hours.^{40–42} Moreover, non-reversible degradation processes can take place in these time frames and under these conditions.^{43,44} An analysis of the spatially resolved transient behavior of PSCs can be found in the [supplemental information](#), section K.

The influence of interfaces on charge extraction

To investigate the effect of the different PSC layers on local extraction of photogenerated charge carriers, a range of spin-coated perovskite cells with an n-i-p structure were studied, for which the optimal layer configuration of glass/transparent conductive oxide (TCO)/electron-extraction layer/perovskite/hole-extraction layer/Au was intentionally altered, using the same materials as for the sample in [Figure 2](#). [Figure 4](#) shows the microscopic images of $PL(V_{oc})$ and $c_{ex}(0)$, respectively, for a solar cell with reduced perovskite layer thickness ([Figure 4A and 4B](#)), a device without electron-extraction layer (EEL) ([Figure 4C and 4D](#)), and one without hole-extraction layer (HEL) ([Figure 4E and 4F](#)). The $c_{ex}(0)$ averaged over the entire image is 0.71, 0.24,

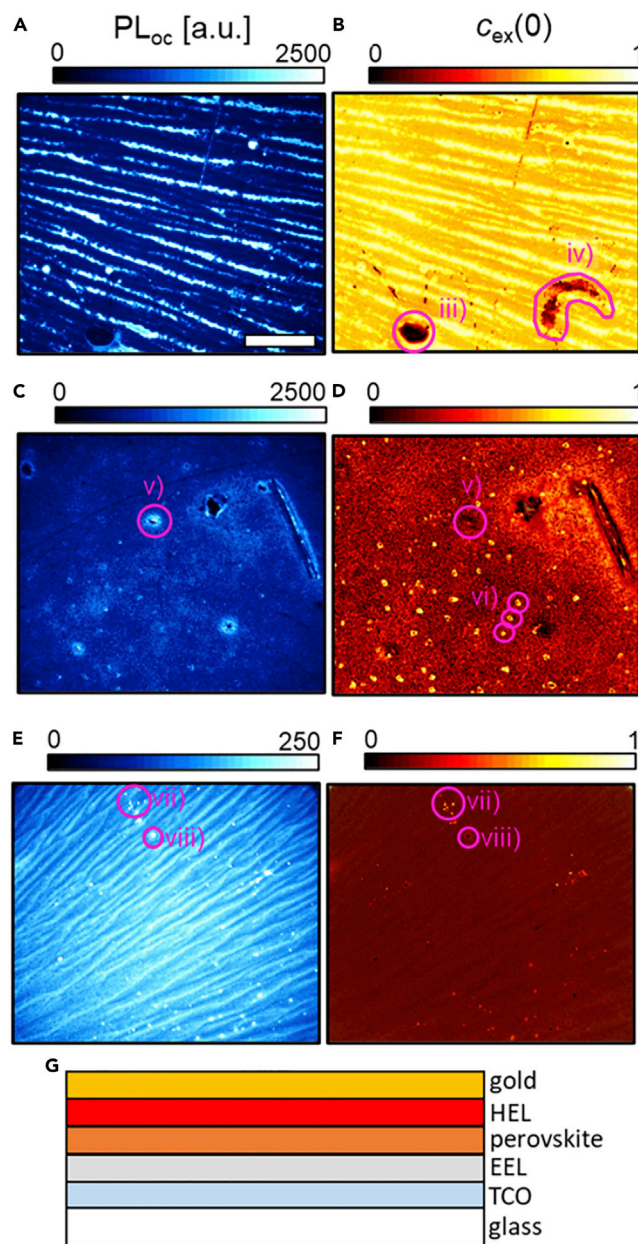


Figure 4. Effect of various layers of a PSC stack on the charge extraction

PL at open circuit ($PL(V_{oc})$, blue images) and charge extraction coefficient ($c_{ex}(0)$, red images) imaging analysis.

(A–F) Three different spin-coated n-i-p PSCs are shown, respectively: a cell with reduced perovskite layer thickness (A and B) as well as an EEL-layer-free (C and D) and an HEL-layer-free device (E and F). Note that the $PL(V_{oc})$ intensity of (A) and (C) ranges up to 2,500 counts, whereas (E) ranges only up to 250 counts. The samples were illuminated with a 632 nm LED light. The scale bar represents 400 μ m for all images.

(G) Illustration of the cell stack, which was illuminated from the bottom. TCO, transparent conductive oxide; EEL, electron-extraction layer; HEL, hole-extraction layer.

and 0.11, respectively. Note that these EEL-free samples displayed comparably low parallel resistances, whereas the HEL-free samples showed high series resistances (cf., [supplemental information](#), section L, [Figure S18](#)). A sketch of the cell stack is displayed in [Figure 4G](#).

The images reveal a range of interesting features and general observations: in [Figures 4A and 4B](#), stripe or wave patterns can be recognized that are most probably caused by the spin-coating process. For these patterns, high $PL(V_{oc})$ correlates with high $c_{ex}(0)$. Comparing the two images furthermore demonstrates that by only employing the $PL(V_{oc})$, some features remain concealed, which become visible in the $c_{ex}(0)$ -representation. In this sense, features (iii) and (iv) in the bottom of the image are most striking, for which the low $c_{ex}(0)$ indicates poor charge extraction. In feature (iii), the $PL(V_{oc})$ is also low, indicating that the perovskite is severely degraded (or absent) at this spot. In contrast, for feature (iv), the $PL(V_{oc})$ is in the same range as for the surroundings, which shows that PV active material is present here. However, the $c_{ex}(0)$ image reveals that the photogenerated charges are not extracted.

Looking at the EEL-free devices in [Figures 4C and 4D](#), we observe an absence of the wave pattern. Hence, this pattern is most probably induced by the spin-coating process of the EEL. Two additional features appear here: similar to feature (i) in [Figure 2](#), feature (v) has a high $PL(V_{oc})$ but a low $c_{ex}(0)$. Inversely, there are many small spots, as represented by three circles for features (vi) that are prominent due to a high $c_{ex}(0)$. In the $PL(V_{oc})$ image, they can, however, not be distinguished from the surrounding regions.

In contrast, the HEL-free devices show the wave-pattern ([Figures 4E and 4F](#)). The $PL(V_{oc})$ is much lower than that of the other samples (note that the color scale was divided by a factor of 10). Also, the $c_{ex}(0)$ is low throughout most of the observed area. There are a few small dots as represented by feature (vii) that display both relatively high $PL(V_{oc})$ and high $c_{ex}(0)$. In contrast, similar to features (i) and (v), feature (viii) shows high $PL(V_{oc})$ but low $c_{ex}(0)$. Further assessments of the effect of the metal back electrode and a comparison of I - V parameters with PL data can be found in the [supplemental information](#), sections M and N.

Identification of charge-extraction loss mechanisms

The measurements presented above demonstrate that the PPI approach is a simple and powerful tool to analyze the local performance of PSCs with microscopic resolution. As the $c_{ex}(0)$ representation also contains information on the local $PL(V_{oc})$ and $PL(V = 0)$, we can use this method, alongside, for instance, PL imaging at open-circuit condition, to unravel interfacial charge-extraction and recombination mechanisms that would not be possible using methods like LBIC alone (cf., the comparison of LBIC, EL, PL, and PPI measurements in the [supplemental information](#), section H). This means that we are not only able to detect regions of low photocurrent but can also estimate why the current is low. Such an investigation is especially significant for the characterization of solution-processed solar cells like PSCs, where a key challenge is the establishment of good electrical coupling between the perovskite crystals and the CELs.⁴⁵

The map in [Figure 5A](#) illustrates how $c_{ex}(0)$ is influenced by the corresponding $PL(V_{oc})$ and $PL(V = 0)$ intensities. A high $c_{ex}(0)$ is achieved if PL is high at open circuit and zero at short circuit. On this map, we can now classify features of the above studied samples within a set of extreme cases.

1. In the ideal case, $c_{ex}(0)$ approaches unity. This means that the non-radiative recombination is minimized, which implies that the radiative recombination is maximized. Practically, this situation is reached if there is full coverage of a high-quality perovskite crystal layer (corresponding to a maximal $PL(V_{oc})$ at open circuit), while the photogenerated charge carriers are ideally extracted

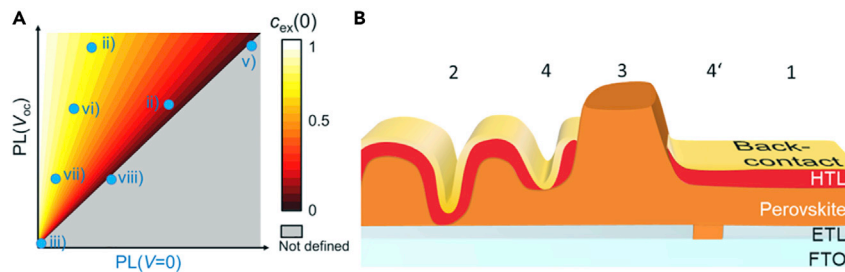


Figure 5. Interpretation of charge-extraction images

(A) Evolution of the charge-extraction coefficient, $c_{ex}(0)$, or normalized local photocurrent, $J_{sc}/J_{gen}|_{PL}$, for different values of PL intensity at open and short circuits. The blue dots correspond to the features from Figures 2 and 4.

(B) Schematic illustration of the cross-section of an n-i-p perovskite solar cell, displaying four characteristic cases for (non-)ideal-charge extraction.

at short circuit. This is represented by the white area at the ordinate of the graph in Figure 5A and by situation (1) in Figure 5B, where a schematic cross-section of a PSC is displayed. Features (ii), (vi), and (vii) approach this ideal situation.

A $c_{ex}(0)$ of zero occurs for two worst-case scenarios:

2. There is no presence of a functional perovskite layer, as for the case of degraded perovskite or even the complete absence of this layer, as depicted by situation (2) in Figure 5B. This situation can be identified if $PL(V_{oc})$ is also zero, as represented by the origin in the graph of Figure 5A. Such a situation can be attributed to feature (iii).
3. A photoactive perovskite layer is present, but there is no charge extraction of the photogenerated charge carriers to the outer terminals. In the most dramatic case, this occurs in the absence of a back electrode, as illustrated by case (3) in Figure 5B. In this case, the PL is not changed at short circuit, and thus $PL(V_{oc}) = PL(V = 0)$, represented by the black area at the bisector in Figure 5A. Due to a lower surface recombination, in practice, the $PL(V_{oc})$ is likely higher in these regions compared with those with good connection to contact layers. Features (i), (v), and (viii) are representative for this situation.
4. Finally, there is also the possibility of poor charge selectivity. This can be the case for an absence of charge-selective layers such that the back or front electrode is directly in contact with the perovskite absorber (case (4, 4') in Figure 5B). Another possibility is a high surface recombination, e.g., due to poor selectivity of the EEL or HEL. In this case, the $PL(V = 0)$ can be zero, but due to high surface recombination, the $PL(V_{oc})$ is also low. The devices without EEL or HEL displayed in Figures 4D and 4F represent such a situation.

Conclusion

The photocurrent-voltage ($J(V)$) curve is the key characteristic to assess PV devices. However, $J(V)$ measurements usually do not contain any spatial information, which are essential for a deeper understanding and further improvements of the devices. A range of methods for the local assessment of the photocurrent have been developed, especially for silicon and III-V solar cells. Yet, none of them has so far been able to offer a combination of local $J(V)$ assessment for all bias voltages between 0 V and V_{OC} and simultaneous fast image acquisition at microscopical resolution.

With the PPI approach proposed in this work, we introduced a straightforward method for a time-resolved assessment of the local PV $J(V)$ curve of PSCs by electrical-bias-dependent luminescence imaging. We derived from basic principles how the measurement of the difference in PL(V) to the PL(V_{OC}) at open circuit can be related to the local $J(V)$ and charge-extraction efficiency. The validity of the approach was experimentally demonstrated by applying it to a close-to-ideal III-V solar cell. Challenges and opportunities of the approach were systematically studied and discussed. By the investigation of a high-performing (PCE >20%) PSC, we showed that the PPI approach allows the real-time assessment of the local assessment of the $J(V)$ curve and the steady-state J_{SC} as well as transient charge-extraction behavior. Furthermore, we demonstrated that the technique also reveals information to assess the local charge-extraction efficiency and interfacial recombination mechanisms. It is therefore a valuable tool for understanding the electrical coupling of the perovskite to the CELs. This work shows that, combined with potentiostatic measurements, microscopic luminescence imaging can be a powerful method to assess performance losses and develop strategies to enhance solar cell performance. The introduced technique can make a significant impact on the understanding and improvement of perovskite and other solar cell technologies as it enables relating morphological artifacts to device performance.

EXPERIMENTAL PROCEDURES

Resource availability

Lead contact

Further information should be directed to the lead contact, Lukas Wagner (lukas.wagner@physik.uni-marburg.de).

Materials availability

This study did not generate new unique reagents.

Data and code availability

Any additional information required to reanalyze the data reported in this paper is available from the [lead contact](#) upon request.

Characterization

The PL intensity was measured in reflectance with an optical microscope at 10-fold magnification. A red and blue high-power LED (Thorlabs Solis) with a peak intensity of 632 and 405 nm, respectively, was used to illuminate the solar cells at a photon flux equivalent to one sun (AM1.5 g), as determined by measuring a reference silicon PV cell and calculating the photon flux from the EQE spectrum. To reach comparable generation current densities, the light intensity was intentionally calibrated to match the photon flux at the corresponding wavelength. This results in an irradiance (i.e., optical power density) of 224 mW/cm² (corresponding to 2.24 suns) for the 623 nm of LED and of 347 mW/cm² (corresponding to 3.47 suns) for the 405 nm LED. On the detector side, the PL light was focused onto a high-resolution sCMOS camera (Andor Zyla 5.5) with an optical high-pass filter (cut off at 760 nm). To apply an electrical bias and to simultaneously measure solar cell currents and voltages, a potentiostat (Ivium CompactStat) was used. After changing the electrical bias, the PL was stabilized for at least 60 s before recording the images of perovskite devices. The exposure time to acquire one PL image was 0.3 s. The solar cells were exposed to ambient laboratory conditions (air, room temperature) during the measurement.

Stabilized current-voltage parameters such as PCE, J_{SC} , and V_{OC} were determined by a class A solar simulator whose intensity was calibrated with a silicon reference cell,

where, for perovskite devices, “stabilized” refers to the value measured after 100 s of measurement. For the determination of the stabilized PCE, the device current was recorded under a fixed bias voltage close to the suspected maximum power point.

Processing parameters of solar cells are outlined in the [supplemental information](#).

SUPPLEMENTAL INFORMATION

Supplemental information can be found online at <https://doi.org/10.1016/j.matt.2022.05.024>.

ACKNOWLEDGMENTS

L.W., J.P.H., S.M., and U.W. acknowledge funding from the European Union’s Horizon 2020 research and innovation program under grant agreement no. 763989 (APOLO). This publication reflects only the author’s views, and the European Union is not liable for any use that may be made of the information contained therein. L.W., M.E., D.B., S.Z., S.M., and A.H. acknowledge funding within the project UNIQUE, supported under the umbrella of SOLAR-ERA.NET_Cofund by ANR, PtJ, MIUR, MINECOAEI, and SWEA. SOLAR-ERA.NET is supported by the European Commission within the EU Framework Program for Research and Innovation HORIZON 2020 (Cofund ERANET Action, no. 691664). P.S. acknowledges funding from the German Ministry of Economic Affairs and Climate Action under the project PoTaSi (0324247). L.W. and D.B. acknowledge scholarship support by the German Federal Environmental Foundation (DBU). P.S. acknowledges his PhD scholarship from the Heinrich Böll Foundation. S.Z. acknowledges scholarship support by the German Academic Exchange Service (DAAD). We thank our colleagues at Fraunhofer ISE, M. Glatthaar for valuable discussions of the PPI method, S. Stättner for support with MOVPE growth, R. Koch for processing of the III-V cell, F. Martin for EQE and reflection measurements of the III-V cell, and E. Fehrenbach for IV measurements of the III-V cell. We further thank T. Pieper (Quantum Design GmbH) for discussion of detector error sources. Finally, we are grateful to the anonymous reviewers for their careful revisions and helpful suggestions that helped to substantially improve the manuscript.

AUTHOR CONTRIBUTIONS

L.W. and A.H. developed the idea of the PPI approach, derived the theory, and conceived the initial measurement. The concept was intensively discussed and the measurement method was refined by the significant contribution of L.W., J.P.H., P.S., M.E., D.B., S.Z., S.M., U.W., A.H., and S.W.G. L.W. wrote the manuscript and developed and carried out PPI measurements and data analysis on III-V devices together with P.S. and on PSCs together with J.P.H., M.E., D.B., and S.Z. Perovskite samples were provided by and data on PSC was discussed with Y.L., S.M.Z., and M.G. III-V samples were fabricated and further characterized by P.S. All authors discussed the results and revised the manuscript.

DECLARATION OF INTERESTS

The authors declare no competing interests.

Received: December 6, 2021

Revised: March 16, 2022

Accepted: May 12, 2022

Published: June 7, 2022

REFERENCES

- Schubert, M.C., Mundt, L.E., Walter, D., Fell, A., and Glunz, S.W. (2020). Spatially resolved performance analysis for perovskite solar cells. *Adv. Energy Mater.* 10, 1904001. <https://doi.org/10.1002/aenm.201904001>.
- Fertig, F., Padilla, M., Breitenstein, O., Höffler, H., Geisemeyer, I., Schubert, M.C., and Rein, S. (2015). Short-circuit current density imaging methods for silicon solar cells. *Energy Proc.* 77, 43–56. <https://doi.org/10.1016/j.egypro.2015.07.008>.
- Mundt, L.E., Kwapił, W., Yakoob, M.A., Herterich, J.P., Kohlstädt, M., Würfel, U., Schubert, M.C., and Glunz, S.W. (2019). Quantitative local loss analysis of blade-coated perovskite solar cells. *IEEE J. Photovolt.* 9, 452–459. <https://doi.org/10.1109/JPHOTOV.2018.2888835>.
- Seager, C.H. (1982). The determination of grain-boundary recombination rates by scanned spot excitation methods. *J. Appl. Phys.* 53, 5968–5971. <https://doi.org/10.1063/1.331389>.
- Padilla, M., Michl, B., Thaidigsmann, B., Warta, W., and Schubert, M.C. (2014). Short-circuit current density mapping for solar cells. *Sol. Energy Mater. Sol. Cells* 120, 282–288. <https://doi.org/10.1016/j.solmat.2013.09.019>.
- Breitenstein, O. (2011). Nondestructive local analysis of current-voltage characteristics of solar cells by lock-in thermography. *Sol. Energy Mater. Sol. Cells* 95, 2933–2936. <https://doi.org/10.1016/j.solmat.2011.05.049>.
- Breitenstein, O., Fertig, F., and Bauer, J. (2015). An empirical method for imaging the short circuit current density in silicon solar cells based on dark lock-in thermography. *Sol. Energy Mater. Sol. Cells* 143, 406–410. <https://doi.org/10.1016/j.solmat.2015.07.027>.
- Fertig, F., Greulich, J., and Rein, S. (2014). Spatially resolved determination of the short-circuit current density of silicon solar cells via lock-in thermography. *Appl. Phys. Lett.* 104, 201111. <https://doi.org/10.1063/1.4876926>.
- Shen, C., Kampwerth, H., Green, M., Thorsten Trupke, T., Carstensen, J., and Schutt, A. (2013). Spatially resolved photoluminescence imaging of essential silicon solar cell parameters and comparison with CELLO measurements. *Sol. Energy Mater. Sol. Cells* 109, 77–81. <https://doi.org/10.1016/j.solmat.2012.10.010>.
- Trupke, T., Pink, E., Bardos, R.A., and Abbott, M.D. (2007). Spatially resolved series resistance of silicon solar cells obtained from luminescence imaging. *Appl. Phys. Lett.* 90, 093506. <https://doi.org/10.1063/1.2709630>.
- Kampwerth, H., Trupke, T., Weber, J.W., and Augarten, Y. (2008). Advanced luminescence based effective series resistance imaging of silicon solar cells. *Appl. Phys. Lett.* 93, 202102. <https://doi.org/10.1063/1.2982588>.
- Glatthaar, M., Haunschild, J., Zeidler, R., Demant, M., Greulich, J., Michl, B., Warta, W., Rein, S., and Preu, R. (2010). Evaluating luminescence based voltage images of silicon solar cells. *J. Appl. Phys.* 108, 014501. <https://doi.org/10.1063/1.3443438>.
- Glatthaar, M., Haunschild, J., Kasemann, M., Giesecke, J., Warta, W., and Rein, S. (2010). Spatially resolved determination of dark saturation current and series resistance of silicon solar cells. *Phys. Status Solidi RRL* 4, 13–15. <https://doi.org/10.1002/pssr.200903290>.
- Breitenstein, O., Höffler, H., and Haunschild, J. (2014). Photoluminescence image evaluation of solar cells based on implied voltage distribution. *Sol. Energy Mater. Sol. Cells* 128, 296–299. <https://doi.org/10.1016/j.solmat.2014.05.040>.
- Haunschild, J., Glatthaar, M., Kasemann, M., Rein, S., and Weber, E.R. (2009). Fast series resistance imaging for silicon solar cells using electroluminescence. *Phys. Status Solidi RRL* 3, 227–229. <https://doi.org/10.1002/pssr.200903175>.
- Hoffler, H., Breitenstein, O., and Haunschild, J. (2015). Short-circuit current density imaging via PL image evaluation based on implied voltage distribution. *IEEE J. Photovolt.* 5, 613–618. <https://doi.org/10.1109/JPHOTOV.2014.2379097>.
- Mastroianni, S., Heinz, F.D., Im, J.-H., Veurman, W., Padilla, M., Schubert, M.C., Würfel, U., Grätzel, M., Park, N.-G., and Hinsch, A. (2015). Analysing the effect of crystal size and structure in highly efficient CH₃NH₃PbI₃ perovskite solar cells by spatially resolved photo- and electroluminescence imaging. *Nanoscale* 7, 19653–19662. <https://doi.org/10.1039/C5NR05308K>.
- Hameiri, Z., Mahboubi Soufiani, A., Juhl, M.K., Jiang, L., Huang, F., Cheng, Y.-B., Kampwerth, H., Weber, J.W., Green, M.A., and Trupke, T. (2015). Photoluminescence and electroluminescence imaging of perovskite solar cells. *Prog. Photovolt. Res. Appl.* 23, 1697–1705. <https://doi.org/10.1002/pip.2716>.
- Okano, M., Endo, M., Wakamiya, A., Yoshita, M., Akiyama, H., and Kanemitsu, Y. (2015). Degradation mechanism of perovskite CH₃NH₃PbI₃ diode devices studied by electroluminescence and photoluminescence imaging spectroscopy. *Appl. Phys. Express* 8, 102302. <https://doi.org/10.7567/APEX.8.102302>.
- Soufiani, A.M., Hameiri, Z., Meyer, S., Lim, S., Tayebjee, M.J.Y., Yun, J.S., Ho-Baillie, A., Conibeer, G.J., Spiccia, L., and Green, M.A. (2016). Lessons learnt from spatially resolved electro- and photoluminescence imaging of interfacial delamination in CH₃NH₃PbI₃ planar perovskite solar cells upon illumination. *Adv. Energy Mater.* 7, 1602111. <https://doi.org/10.1002/aenm.201602111>.
- Stolterfoht, M., Le Corre, V.M., Feuerstein, M., Caprioglio, P., Koster, L.J.A., and Neher, D. (2019). Voltage-dependent photoluminescence and how it correlates with the fill factor and open-circuit voltage in perovskite solar cells. *ACS Energy Lett.* 4, 2887–2892. <https://doi.org/10.1021/acsenenergylett.9b02262>.
- Mundt, L.E., Heinz, F.D., Albrecht, S., Mundus, M., Saliba, M., Correa-Baena, J.P., Anaraki, E.H., Korte, L., Grätzel, M., Hagfeldt, A., et al. (2017). Nondestructive probing of perovskite silicon tandem solar cells using multiwavelength photoluminescence mapping. *IEEE J. Photovolt.* 7, 1081–1086. <https://doi.org/10.1109/JPHOTOV.2017.2688022>.
- Walter, D., Yiliang Wu, Y., Duong, T., Peng, J., Jiang, L., Fong, K.C., and Weber, K. (2017). On the use of luminescence intensity images for quantified characterization of perovskite solar cells. Spatial distribution of series resistance. *Adv. Energy Mater.* 8, 1701522. <https://doi.org/10.1002/aenm.201701522>.
- Rietwyk, K.J., Tan, B., Surmiak, A., Lu, J., McMeekin, D.P., Raga, S.R., Duffy, N., and Bach, U. (2020). Light intensity modulated photoluminescence for rapid series resistance mapping of perovskite solar cells. *Nano Energy* 73, 104755. <https://doi.org/10.1016/j.nanoen.2020.104755>.
- Soufiani, A.M., Kim, J., Ho-Baillie, A., Green, M., and Hameiri, Z. (2018). Luminescence imaging characterization of perovskite solar cells: a note on the analysis and reporting the results. *Adv. Energy Mater.* 8, 1702256. <https://doi.org/10.1002/aenm.201702256>.
- Leblebici, S.Y., Leppert, L., Li, Y., Reyes-Lillo, S.E., Wickenburg, S., Wong, E., Lee, J., Melli, M., Ziegler, D., Angell, D.K., et al. (2016). Facet-dependent photovoltaic efficiency variations in single grains of hybrid halide perovskite. *Nat. Energy* 1, 16093. <https://doi.org/10.1038/nenergy.2016.93>.
- Weber, S.A.L., Hermes, I.M., Turren-Cruz, S.-H., Gort, C., Bergmann, V.W., Gilson, L., Hagfeldt, A., Graetzel, M., Tress, W., and Berger, R. (2018). How the formation of interfacial charge causes hysteresis in perovskite solar cells. *Energy Environ. Sci.* 11, 2404–2413. <https://doi.org/10.1039/C8EE01447G>.
- Li, J., Huang, B., Nasr Esfahani, E., Wei, L., Yao, J., Zhao, J., and Chen, W. (2017). Touching is believing: interrogating halide perovskite solar cells at the nanoscale via scanning probe microscopy. *npj Quant. Mater.* 2, 56. <https://doi.org/10.1038/s41535-017-0061-4>.
- Song, J., Zhou, Y., Padture, N.P., and Huey, B.D. (2020). Anomalous 3D nanoscale photoconduction in hybrid perovskite semiconductors revealed by tomographic atomic force microscopy. *Nat. Commun.* 11, 3308. <https://doi.org/10.1038/s41467-020-17012-y>.
- Donolato, C. (1985). A reciprocity theorem for charge collection. *Ultramicroscopy* 46, 270–272. <https://doi.org/10.1063/1.95654>.
- Rau, U. (2007). Reciprocity relation between photovoltaic quantum efficiency and electroluminescent emission of solar cells. *Phys. Rev. B* 76, 085303–085308. <https://doi.org/10.1103/PhysRevB.76.085303>.
- Wong, J., and Green, M.A. (2012). From junction to terminal: extended reciprocity relations in solar cell operation. *Phys. Rev. B* 85, 235205. <https://doi.org/10.1103/PhysRevB.85.235205>.
- Rau, U., Blank, B., Müller, T.C.M., and Kirchartz, T. (2017). Efficiency potential of photovoltaic materials and devices unveiled by detailed-balance analysis. *Phys. Rev. Appl.* 7, 044016.

- <https://doi.org/10.1103/PhysRevApplied.7.044016>.
34. Kirchartz, T., and Rau, U. (2018). What makes a good solar cell? *Adv. Energy Mater.* 8, 1703385. <https://doi.org/10.1002/aenm.201703385>.
35. Green, M., Dunlop, E., Hohl-Ebinger, J., Yoshita, M., Kopidakis, N., and Hao, X. (2021). Solar cell efficiency tables (version 57). *Prog. Photovolt. Res. Appl.* 29, 3–15. <https://doi.org/10.1002/pip.3371>.
36. Kayes, B.M., Nie, H., Twist, R., Spruytte, S.G., Reinhardt, F., Kizilyalli, I.C., and Higashi, G.S. (2011). 27.6% conversion efficiency, a new record for single-junction solar cells under 1 sun illumination. In 37th IEEE Photovoltaic Specialists Conference, pp. 4–8. <https://doi.org/10.1109/PVSC.2011.6185831>.
37. Geisz, J.F., France, R.M., Schulte, K.L., Steiner, M.A., Norman, A.G., Guthrey, H.L., Young, M.R., Song, T., and Moriarty, T. (2020). Six-junction III–V solar cells with 47.1% conversion efficiency under 143 Suns concentration. *Nat. Energy* 5, 326–335. <https://doi.org/10.1038/s41560-020-0598-5>.
38. Tennyson, E.M., Doherty, T.A.S., and Stranks, S.D. (2019). Heterogeneity at multiple length scales in halide perovskite semiconductors. *Nat. Rev. Mater.* 4, 573–587. <https://doi.org/10.1038/s41578-019-0125-0>.
39. Mahboubi Soufiani, A., Zhu, Y., Mussakhanuly, N., Yun, J.S., Trupke, T., and Hameiri, Z. (2021). Contactless series resistance imaging of perovskite solar cells via inhomogeneous illumination. *Sol. RRL* 5, 2100655. <https://doi.org/10.1002/solr.202100655>.
40. Xu, Z., De Rosia, T., and Weeks, K. (2017). Photoluminescence–voltage (PL–V) hysteresis of perovskite solar cells. *J. Phys. Chem. C* 121, 24389–24396. <https://doi.org/10.1021/acs.jpcc.7b06711>.
41. Chen, S., Wen, X., Huang, S., Huang, F., Cheng, Y.-B., Green, M., and Ho-Baillie, A. (2017). Light illumination induced photoluminescence enhancement and quenching in lead halide perovskite. *Sol. RRL* 1, 1600001. <https://doi.org/10.1002/solr.201600001>.
42. Howard, J.M., Tennyson, E.M., Barik, S., Szostak, R., Waks, E., Toney, M.F., Nogueira, A.F., Neves, B.R.A., and Leite, M.S. (2018). Humidity-induced photoluminescence hysteresis in variable Cs/Br ratio hybrid perovskites. *J. Phys. Chem. Lett.* 9, 3463–3469. <https://doi.org/10.1021/acs.jpclett.8b01357>.
43. Khenkin, M.V., K. M., A., Visoly-Fisher, I., Kolusheva, S., Galagan, Y., Di Giacomo, F., Vukovic, O., Patil, B.R., Sherafatipour, G., Turkovic, V., et al. (2018). Dynamics of photoinduced degradation of perovskite photovoltaics: from reversible to irreversible processes. *ACS Appl. Energy Mater.* 1, 799–806. <https://doi.org/10.1021/acsaem.7b00256>.
44. Gomez, A., Sanchez, S., Campoy-Quiles, M., and Abate, A. (2018). Topological distribution of reversible and non-reversible degradation in perovskite solar cells. *Nano Energy* 45, 94–100. <https://doi.org/10.1016/j.nanoen.2017.12.040>.
45. Wagner, L., Mundt, L.E., Mathiazhagan, G., Mundus, M., Schubert, M.C., Mastroianni, S., Würfel, U., Hinsch, A., and Glunz, S.W. (2017). Distinguishing crystallization stages and their influence on quantum efficiency during perovskite solar cell formation in real-time. *Sci. Rep.* 7, 14899. <https://doi.org/10.1038/s41598-017-13855-6>.